Antarctic atmospheric Richardson number from radiosoundings measurements and AMPS

Qike Yang[1,2,3], Xiaoqing Wu[1,2,3], Xiaodan Hu[1,2,3], Zhiyuan Wang[1,3], Chun Qing[1,2,3], Tao Luo[1,2,3], Pengfei Wu[1,2,3], Xianmei Qian[1,2,3], and Yiming Guo[1,2,3]

[1]Key Laboratory of Atmospheric Optics, Anhui Institute of Optics and Fine Mechanics, HFIPS, Chinese Academy of Sciences, Hefei 230031, China
[2]Science Island Branch of Graduate School, University of Science and Technology of China, Hefei 230026, China
[3]Advanced Laser Technology Laboratory of Anhui Province, Hefei 230037, China

Correspondence: Xiaoqing Wu (xqwu@aiofm.ac.cn)

Abstract. Monitoring a wide range of atmospheric turbulence over the Antarctic continent is still tricky, while the atmospheric Richardson number (Ri; a valuable parameter which determines the possibility that turbulence could be triggered) is easier to obtain. The Antarctic atmospheric Ri, calculated from the potential temperature and wind speed, was investigated using the daily results from the radiosoundings and forecasts of the Antarctic Mesoscale Prediction System (AMPS). Radiosoundings for a year at three sites (McMurdo, South Pole, and Dome C) were used to quantify the reliability of the AMPS forecasts. The AMPS-forecasted Ri can identify the main spatiotemporal characteristics of atmospheric turbulence over the Antarctic region. The correlation coefficients (R_{xy}) of $\log_{10}(Ri)$ at McMurdo, the South Pole, and Dome C are 0.71, 0.59, and 0.53, respectively. The Ri was generally underestimated by the AMPS and the AMPS could better capture the trend of $\log_{10}(Ri)$ at relatively unstable atmospheric conditions. The seasonal median of $\log_{10}(Ri)$ along two vertical cross-sections of the AMPS forecasts are presented, and it shows some zones where atmospheric turbulence can be highly triggered in Antarctica. The Ri distributions appear to be reasonably correlated to some large-scale phenomena or local-scale dynamics (katabatic winds, polar vortices, convection, gravity wave, etc) over the Antarctic plateau and surrounding ocean. Finally, the $\log_{10}(Ri)$ at the planetary boundary layer height ($PBLH$) were calculated and their median value is 0.316, this median value, in turn, was used to estimate $PBLH$ and agree well with the AMPS-forecasted $PBLH$ ($R_{xy} > 0.69$). Overall, our results suggest that the estimated Ri by AMPS are reasonable and the turbulence conditions in Antarctica are well revealed.

1 Introduction

The Richardson number (Ri) is a valuable parameter for giving insight into atmospheric stability; it combines both thermodynamic and dynamic profiles, which can indirectly characterize turbulent heat fluxes (Town and Walden, 2009) and optical turbulence (Yang et al., 2021, 2022) in Antarctica. However, the measurements of atmospheric properties in Antarctica are sparse compared to those in the mid-latitudes and tropics. Atmospheric models have been developed to overcome this limitation (Meso-NH by Lascaux et al., 2009; Polar WRF by Bromwich et al., 2013; MAR by Gallée et al., 2015), allowing researchers to investigate atmospheric variability beyond observational coverage, even for forecasting atmospheric parame-

ters in the future. The Antarctic Mesoscale Prediction System (AMPS; https://www2.mmm.ucar.edu/rt/amps/) runs a real-time atmospheric model and provides numerical forecasts for Antarctica. The performances of AMPS in forecasting temperature, wind, precipitable water vapor, cloud, radiation, and heat flux have been examined in previous studies (Monaghan et al., 2005; Seefeldt et al., 2011; Vázquez B and Grejner-Brzezinska, 2012; Wille et al., 2016; Listowski and Lachlan-Cope, 2017; Hines et al., 2019). To our knowledge, using the AMPS to forecast Ri has not been formally validated. Thus, this study will investigate the reliability of the estimated Ri using AMPS forecasts. The atmospheric model employed for AMPS is the Polar version of the Weather Research and Forecasting (Polar WRF) model (Powers et al., 2012). Polar WRF (http://polarmet.osu.edu/PWRF/) has been modified for use in polar regions, for example, improving the representation of heat transfer through snow and ice (Hines and Bromwich, 2008; Hines et al., 2015). The Polar WRF has been used to simulate the Ri at Dome A in Antarctica, and the simulated Ri behaved as expected since the Ri is generally large when the disturbance effects of atmospheric turbulence on wave propagation (optical turbulence) are weak (Yang et al., 2021). Besides, the Polar WRF simulated Ri performed well in estimating boundary layer height when compared with other methods (Yang et al., 2022).

Presently, monitoring a wide range of atmospheric turbulence over the Antarctic continent is tremendously difficult, but atmospheric Ri is easier to obtain, as it can be calculated from the routine meteorological parameters (potential temperature and wind speed). However, few studies have evaluated atmospheric models to forecast Ri in Antarctica, because of limited meteorological experiments here. Nevertheless, Geissler and Masciadri (2006) and Hagelin et al. (2008) used the European Centre for Medium-Range Weather Forecasts (ECMWF) analyses to calculate atmospheric Ri in Antarctica. The ECMWF analyses were generated from the data assimilation using observations (P. Lönnberg, 1992), and can provide initial states for numerical models (such as Polar WRF). However, their research has some specific shortcomings (or problems that need further study): (1) They did not compare Ri estimations from forecasts and measurements, while the forecast function is of great significance for practical application (e.g., astronomical observations, aviation safety, optical communication, etc). (2) How model errors of Ri depend on atmospheric conditions has not been analyzed. (3) The correlations between turbulence conditions (indicated by Ri) and some large-scale phenomena or local-scale dynamics in Antarctica were not fully investigated. (4) A reference standard for judging the probability of triggering turbulence using the model-estimated Ri was not given. To fill these gaps, the scientific goals of this paper are thus as follows:

1. To carry out a detailed comparison of potential temperature and wind speed (on which Ri depends) in the atmospheric column, this study extends the model evaluations above two sites (Hagelin et al., 2008) to three sites (McMurdo, South Pole, and Dome C) over the Antarctic continent for an entire year. The three sites are considered representative, as the coast (McMurdo), flank (South Pole), and summit (Dome C) of the Antarctic continent will be compared using radiosoundings and AMPS forecasts.

2. The radiosonde can measure meteorological parameters, which can estimate Ri. Using the AMPS-forecasted meteorological parameters, one also can obtain the Ri. Then, a comparison of Ri estimated from measurements and forecasts can be achieved, allowing us to evaluate the reliability of AMPS-forecasted Ri in giving insight into the atmospheric turbulence in Antarctica. In addition, we investigated how the discrepancies between the models and measurements depend on the atmospheric conditions.

3. Two vertical cross-sections for Ri will be given, which may provide a better perspective on the turbulence conditions in both vertical and horizontal dimensions, instead of only focusing on the vertical dimension (or atmospheric column; e.g., Geissler and Masciadri, 2006; Hagelin et al., 2008). This will help to identify regions and periods that are favorable for triggering atmospheric turbulence in Antarctica. Moreover, this will enable us to correlate the Ri distribution with some large-scale phenomena or local-scale dynamics (katabatic winds, polar vortices, convection, gravity wave, etc.) in Antarctica, and the underlying physical processes of Antarctic atmospheric turbulence will be investigated.

4. The Planetary Boundary Layer Height ($PBLH$, within which the atmosphere is generally turbulent) can be estimated using a critical value of Ri, typically 0.25 (Holtslag et al., 1990; Pietroni et al., 2012; Petenko et al., 2019). However, this critical value depends on the vertical resolution of data (Troen and Mahrt, 1986; Holtslag et al., 1990), and may be different for the AMPS grid resolution. Then the Ri at the AMPS-forecasted $PBLH$ (Ri_{PBLH}) was obtained as a reference standard for judging whether the atmosphere is likely to be laminar flow ($Ri>Ri_{PBLH}$) or turbulent flow ($Ri<Ri_{PBLH}$) when using the AMPS-forecasted Ri.

In Sect. 2, we present the experimental data and atmospheric model used in this study, with an explanation of their main features. In Sect. 3, the Ri is introduced. In Sect. 4, we compare AMPS forecasts to radiosoundings and analyze the atmospheric turbulence conditions in Antarctica. Sect. 5 summarizes the main findings and primary takeaways of this study.

2 Data and model

2.1 Radiosoundings

Daily radiosounding measurements at McMurdo (MM) and the South Pole (SP) are available at the Antarctic Meteorological Research Center (AMRC; ftp://amrc.ssec.wisc.edu/pub). For Dome C (DC), one can obtain the measurements at the Antarctic Meteo-Climatological Observatory (http://www.climantartide.it). The altitudes of the three sites are 9 m (MM), 2839 m (SP), and 3239 m (DC), where the altitudes correspond to the heights of the radiosondes at the time of launch. Their locations are shown in Fig. 1. Dome A (DA) is also marked in Fig. 1, which is the highest location (4083 m) on the Antarctic plateau and the atmospheric conditions above it will also be analyzed in this study (see Sect. 4.2.3). The radiosonde-measured meteorological parameters include pressure, temperature, wind speed, and wind direction; one year (from 2021 March to 2022 February) of these meteorological parameters was used in this study. Generally, the radiosonde was launched once a day at the same hour (sometimes twice a day at MM and SP). In total, 518, 508, and 340 profiles are available at MM, SP, and DC from 2021 March to 2022 February.

The radiosonde instrumentation used during this measurement period was the Vaisala RS41 (Technical data: https://www.vaisala.com/en/products/weather-environmental-sensors/upper-air-radiosondes-rs41). The accuracy and uncertainty of the radiosonde measurements are listed in Table 1. The radiosondes measure the atmosphere between the ground and an altitude of 10–25 km (low in winter and high in summer) with a typical ascent rate of 5 m s^{-1}, and a logging frequency of 1 Hz; then the vertical resolution is approximately 5 m.

Table 1. Main technical specifications of the radiosonde RS41.

Measuring element	System resolution	System uncertainty	Data resolution*
Temperature	0.01°C	0.15°C (> 100 hPa)	0.1°C
		0.30°C (<100 hPa)	
Pressure	0.01 hPa	0.5 hPa (> 100 hPa)	0.1 hPa
		0.3 hPa (3-100 hPa)	
Wind speed	0.1 m s^{-1}	0.15 m s^{-1}	0.1 m s^{-1} (McMurdo)
			0.1 kts (South Pole)
			0.1 m s^{-1} (Dome C)
Wind Direction	0.1 deg	2 deg	0.1 deg (McMurdo)
			1 deg (South Pole)
			1 deg (Dome C)

*Resolution in the files that are available for download from the Web (ftp://amrc.ssec.wisc.edu/pub, http://www.climantartide.it).
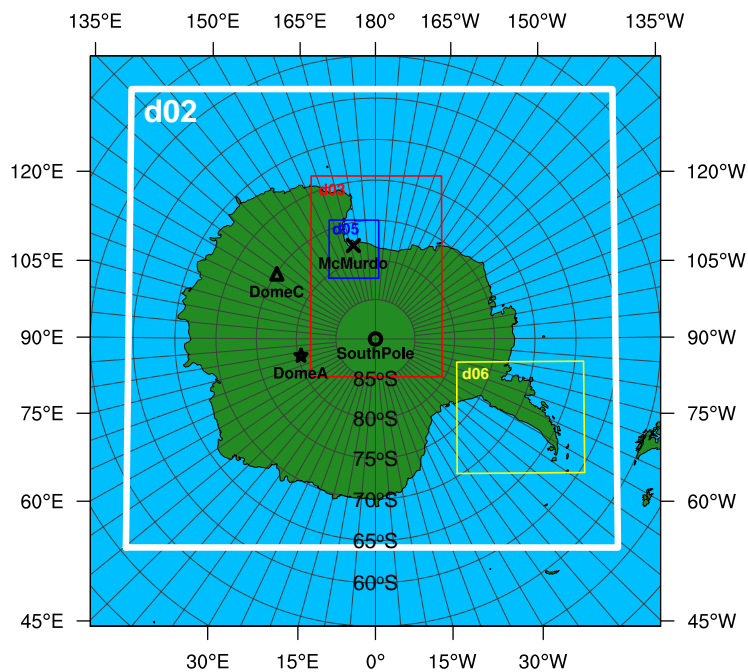
Figure 1. The five two-way interactive horizontal grids (d01, d02, d03, d05, and d06; information online at https://www2.mmm.ucar.edu/rt/amps/information/configuration/maps_2017101012/maps.html) used in the AMPS configuration. The locations of McMurdo (78°S, 167°E), South Pole (90°S, …°E), Dome C (75°S, 123°E), and Dome A (80°S, 78°E) are shown by the cross, circle, triangle, and star, respectively.

2.2 AMPS

The AMPS can forecast meteorological parameters in four-dimensional space-time in Antarctica, which can be used for comparison with the radiosonde measurements. The AMPS grid system consisted of a series of nested domains with 60 vertical levels. This study used grid 2 fields (d02; 8 km horizontal resolution) that covered the entire Antarctic continent (similar to Hines et al., 2019), as shown by the white square in Fig. 1. However, the contributions from the nested grid with higher horizontal resolution (d03: 2.67 km; d05: 0.89 km; d06: 2.67 km) are not entirely lost, as the AMPS used a two-way nested run and the nest (e.g., d03) feeds its calculation back to the coarser domain (e.g., d02). The original WRF output files for each AMPS grid were saved in a rolling archive (one can find how to download the original WRF output files at https://www2.mmm.ucar.edu/rt/amps/information/amps_esg_data_info.html). This study used the AMPS outputs (in original WRF format) from the daily AMPS forecasts that began at 12:00 UTC. Parish and Waight (1987) showed large adjustments to the boundary layer fields above an ice sheet before the numerical model began to stabilize after about 10 h. Then, some studies (Hines and Bromwich, 2008; Hines et al., 2019) have discarded the first 12 h forecasts (so-called 12 h spin-up time). Thus, in this study, only the 12-33-h forecasts from each of the AMPS simulations are combined into a year-long (2011 March to 2022 February) output field at 3-h intervals.

3 Theory of Richardson number

The Ri is generally defined as (Richardson and Shaw, 1920; Chan, 2008):

$$Ri = \frac{g}{\theta} \frac{\partial\theta/\partial z}{\left[\partial u/\partial z\right]^2 + \left[\partial v/\partial z\right]^2} \tag{1}$$

Where g is the gravitational acceleration (9.8 m s^{-2}), $\theta = T[1000/P]^{0.286}$ is the potential temperature (K), T and P are the temperature (K) and pressure (hPa) of air, respectively. As for wind shear term, u and v are the east-west and north-south components of the wind (m s^{-1}). z is the height (m) above the ground. To calculate Ri, a centered finite difference operation was used to estimate the gradient in Eq. (1).

The development of atmospheric turbulence was shown to be tightly correlated with the Ri. It can, therefore, be an essential indicator of the turbulence characteristics in the atmosphere (Ma et al., 2020; Han et al., 2021; Yang et al., 2021). Atmospheric conditions are favorable for the occurrence of turbulence when Ri is less than a critical value (Ri_c), and Ri_c is typically chosen as 0.25. However, a larger Ri_c should be used in a large-scale model (e.g., 0.5 has been employed by Troen and Mahrt, 1986).

In the results of this study, the logarithm of Ri, $\log_{10}(Ri)$, is presented instead of Ri itself, because Ri can vary by two or more orders of magnitude in the atmosphere.

4 Results and discussion

4.1 Potential temperature and wind speed

The AMPS forecasts are compared to radiosoundings from MM, SP, and DC to investigate the reliability of the AMPS forecasts
over the Antarctic continent. The radiosoundings and AMPS forecasts used for this comparison were obtained from 2021
March to 2022 February. To offer a more convincing result, data corresponding to the altitude at which radiosoundings reached
less than five times a season were discarded. In addition, the extracted AMPS forecasts used for comparison were from the
nearest grid to the three sites, and the time difference between radiosoundings and AMPS forecasts larger than 1.5 hours
was not used for comparison. Moreover, both radiosoundings and AMPS forecasts were linearly interpolated to the same
height series for each site. Such height series is the average annual altitude of the AMPS vertical grid, as the altitude of the
AMPS grid may vary during the simulation as the AMPS uses the WRF hybrid vertical coordinate, see information online at
https://www2.mmm.ucar.edu/wrf/users/docs/user_guide_v4/WRFUsersGuide.pdf. On the other hand, it should be noted that
the near-surface radiosonde measurements could be less reliable, as it was just released from the operator's hand (or some
machine). Hagelin et al. (2008) conclude that the radiosoundings are ∼1 K colder than the Automatic Weather Station at Dome
C and ∼2 K at the South Pole. In this study, the radiosonde measurements in the first ∼10 m above the ground were not used.
This is also because the first AMPS grid is ∼10 m above the ground.
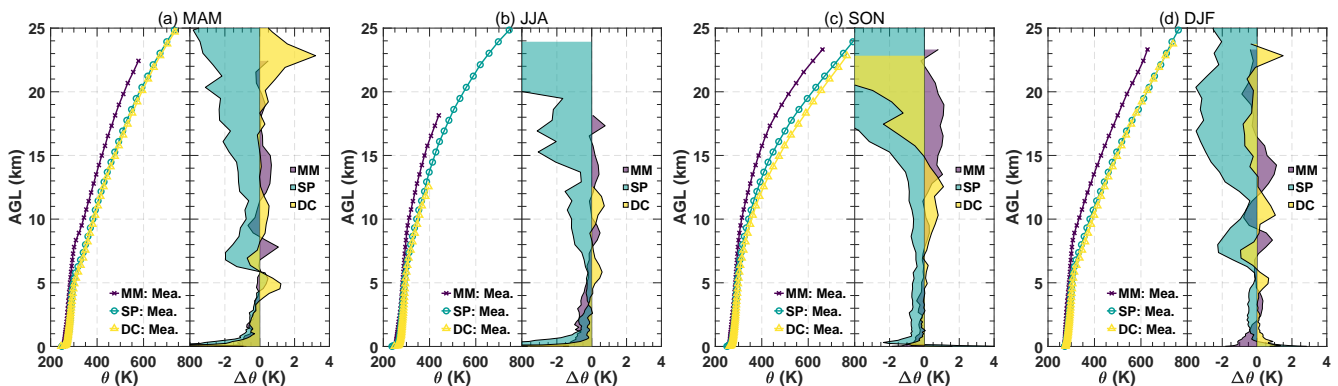
Figure 2. The seasonal median of potential temperature (θ) estimated by the radiosonde measurements (solid lines) and potential temperature
difference ($\Delta\theta$) calculated by the AMPS forecasts minus the radiosonde measurements, i.e. $\Delta\theta=\theta_{AMPS} - \theta_{Mea.}$ (filled areas). Fall: March-
May (MAM); winter: June-August (JJA); spring: September-November (SON); summer: December-February (DJF).

The seasonal median difference of potential temperature (see the filled areas in Fig. 2) and wind speed (see the filled areas in
Fig. 3) between radiosoundings and AMPS forecasts are presented. The missing value of median difference in the upper part
of the atmosphere during JJA indicates that the radiosonde balloon does not reach as high an AGL (Above Ground Level) in
winter as they do in summer, probably because the elastic material of the balloons is more fragile in cold seasons and easier to
explode (Hagelin et al., 2008). The lack of measurements may be attributable to some large values of the median difference in
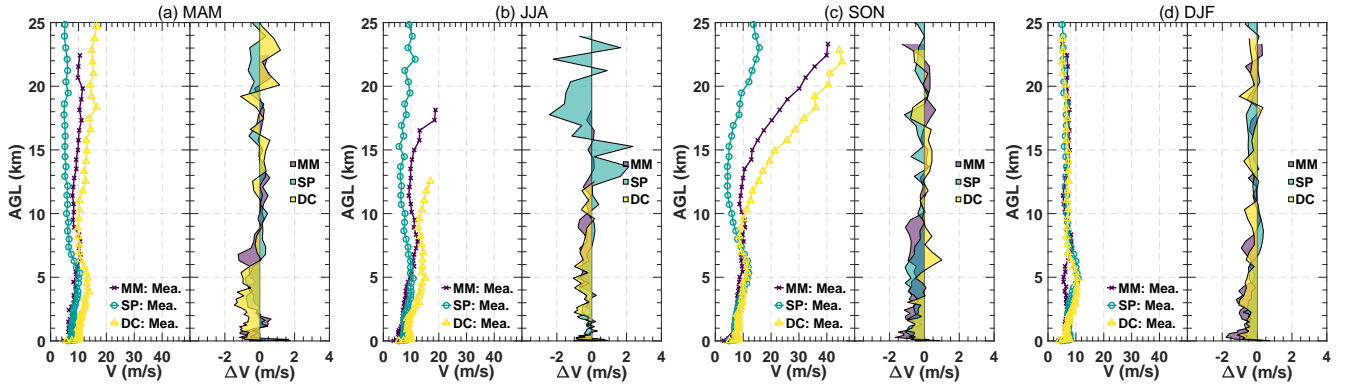
Figure 3. As in Fig. 2, but for wind speed V ($=\sqrt{u^2+v^2}$), and $\Delta V=V_{AMPS}-V_{Mea.}$.

the top layer of the profile shown in Fig. 2 and 3, as the AMPS requires the assimilation data from measurements to initialize its numerical model, and the lack of measurements makes it more difficult for AMPS to simulate atmospheric changes that are close to reality.

140   Fig. 2 shows that the median difference for θ is of the order of 1 K in the first 5 km, except for the atmosphere layer in proximity to the ground. Above 5 km, the AMPS has obviously underestimated the θ at MM, while the forecasts at SP and DC are closer to measurements. Fig. 3 shows that the measured wind speed profiles above 10 km at MM and DC are stronger during spring, indicating the occurrence of the Antarctic polar vortex (Boville et al., 1988). However, the change in wind speed above SP is not that obvious, because the Antarctic vortex is roughly pole-centered (Karpetchko et al., 2005). From the filled areas

145   in Fig. 3, the AMPS forecasts appear consistent with the measurements, as the median difference in wind speed is generally ~1 m s^{-1} and has barely exceeded 2 m s^{-1}, whether the wind is strong or weak. In the first 10 km, most ΔV at the three sites are less than 0, suggesting that the AMPS underestimated the wind speed. Table 2 shows the statistical evaluations of θ and V forecasted by the AMPS. It seems the AMPS can well capture the trend of θ and V as the correlation coefficient (R_{xy}) are all larger than 0.84.

150   **4.2   Richardson number**

4.2.1   Statistical analysis

To evaluate the performance of AMPS in forecasting the possibility of triggering turbulence over the Antarctic continent, the Ri estimations between radiosoundings and AMPS forecasts will be compared. The calculated value of Ri depends on the vertical resolution of meteorological parameters (Troen and Mahrt, 1986; Holtslag et al., 1990). Thus, the meteorologi-

155   cal parameters from the radiosoundings and AMPS forecasts were interpolated into the same height series (as mentioned in Sect. 4.1) to calculate Ri. Where $\partial\theta/\partial z$ and $(\partial u/\partial z)^2+(\partial v/\partial z)^2$ for calculating Ri (see Eq. (1)) were both computed using a centered finite difference operation, as we found that centered difference performed better than forward difference and

backward difference (not shown), i.e., better consistency of Ri between radiosoundings and AMPS forecasts can be achieved using centered difference.
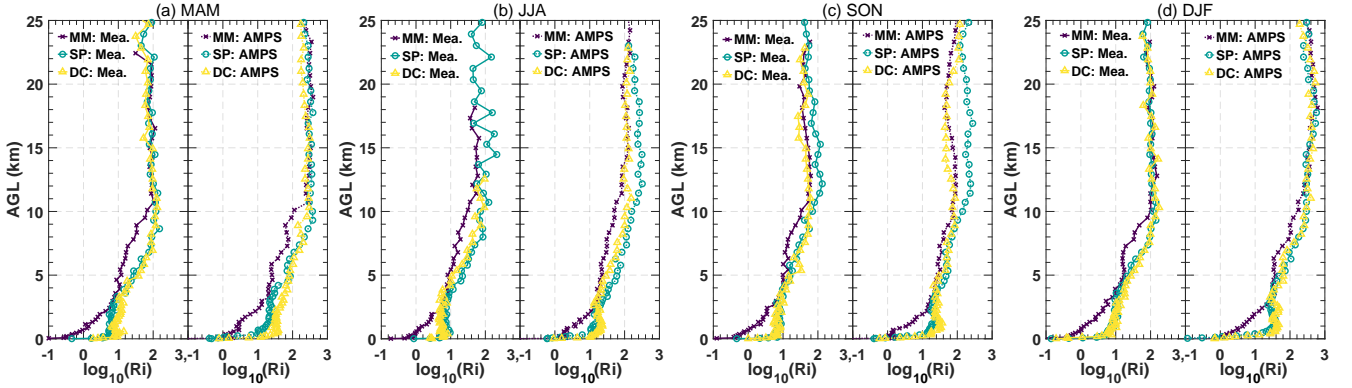
Figure 4. The seasonal median of $\log_{10}(Ri)$ estimated by the AMPS forecasts (solid lines) and the radiosonde measurements (dashed lines).

160   The seasonal median profiles of $\log_{10}(Ri)$ from radiosoundings and AMPS forecasts are shown in Fig. 4. However, the median differences are not presented like the θ and V. This is because, the Ri value can vary massively (by two or more orders of magnitude) in the atmosphere, and a precise quantification seems less plausible. Considering this, we initially intended to examine whether AMPS can reconstruct an accurate shape of $\log_{10}(Ri)$ profile, while median difference is not suitable for this purpose, and the results from radiosoundings and AMPS forecasts are both presented. Nevertheless, the model biases is
165   by all means of great significance, and it will be discussed later (see Table 2 and Fig. 6). In Fig. 4, one can see that the AMPS-forecasted Ri can identify that the atmosphere above MM tends to be more turbulent (Ri is smaller) than SP and DC. In the vertical height direction, the AMPS forecasts can roughly capture the height that can easily trigger turbulence. For example, one can observe that the Ri from radiosoundings and AMPS forecasts both show small values very close to the ground at DC and the SP, which is per the fact that strong atmospheric turbulence is concentrated within the surface layer above the high
170   plateau (Marks et al., 1999; Agabi et al., 2006). A very calm atmosphere (Ri is large) at high altitudes is also consistent with the results given by Travouillon et al. (2003), Aristidi et al. (2005), Trinquet et al. (2008), and Vernin et al. (2009). On the other hand, the AMPS can well reconstruct the near-ground "convex-concave–convex" (hereafter "C-C-C") shaped $\log_{10}(Ri)$ profiles indicated by the radiosonde measurements (see more details in Fig. 5). In terms of time, the AMPS can forecast that the free-atmosphere Ri decreased during spring (SON), this decrease is obvious for MM and DC, where the wind speed are
175   significantly stronger during SON, as in Fig. 3.

Quantitative analysis for the estimated Ri from the numerical models was generally missed as it always varies dramatically, e.g. Hagelin et al. (2008), who focused on the qualitative analysis. Nevertheless, quantitative analysis has been tried in this study since that can give a precise evaluation of the forecast ability of AMPS. Then, the R_{xy}, mean bias ($Bias$; AMPS-radiosonde), and root mean square error ($RMSE$) are calculated using the combined data of all profiles for each season. Where the time

Table 2. Statistical evaluations of the potential temperature (θ), wind speed (V), and logarithmic Richardson number ($\log_{10}(Ri)$) forecasted by the AMPS when compared with the results from radiosonde measurements.

	McMurdo				South Pole				Dome C			
Season	MAM	JJA	SON	DJF	MAM	JJA	SON	DJF	MAM	JJA	SON	DJF
θ: R_{xy}	0.99	0.99	0.99	0.99	0.99	0.99	0.99	0.99	0.99	0.99	0.99	0.99
θ: $Bias$	-0.32	-0.61	-0.10	-0.23	-1.30	-1.41	-1.45	-0.94	-0.74	-0.58	-0.25	0.19
θ: $RMSE$	1.82	1.91	1.78	1.56	2.65	2.88	3.48	2.43	4.28	2.22	2.38	1.76
V: R_{xy}	0.85	0.89	0.95	0.90	0.86	0.84	0.89	0.90	0.92	0.92	0.97	0.95
V: $Bias$	-0.25	-0.25	-0.59	-0.67	-0.16	-0.29	-0.64	-0.40	-0.62	-0.43	-0.24	-0.50
V: $RMSE$	3.16	3.63	3.23	2.81	2.52	2.90	2.69	2.37	2.50	2.94	2.69	1.89
$\log_{10}(Ri)$: R_{xy}	0.75	0.65	0.68	0.77	0.61	0.50	0.56	0.70	0.51	0.45	0.50	0.66
$\log_{10}(Ri)$: $Bias$	0.41	0.32	0.33	0.47	0.36	0.23	0.29	0.35	0.45	0.39	0.30	0.46
$\log_{10}(Ri)$: $RMSE$	0.90	0.86	0.88	0.93	0.90	0.84	0.85	0.90	0.93	0.86	0.81	0.91

180   difference between radiosoundings and AMPS forecasts was limited to less than 1.5 hours. Finally, the seasonal values of the three statistical operators are calculated, as listed in Table 2. However, we want to emphasize that one should focus on the value of R_{xy} that reflects the tendency, instead of $Bias$ and $RMSE$, as a precise quantification remains in doubt (Hagelin et al., 2008). The mean values of R_{xy} for MM, SP, and DC over four seasons are 0.71, 0.59, and 0.53, respectively. The highest R_{xy} is at MM for DJF (0.77) and the lowest is at DC for JJA (0.45). We found that these two cases correspond to the most unstable

185   and stable atmospheric conditions, their median $[\theta_{1000m}\text{-}\theta_{0m}]/[1000m - 0m]$ equal to 0.0038 and 0.0721, respectively. This suggests that the AMPS can better capture the trend of $\log_{10}(Ri)$ at a relatively unstable atmosphere. However, the $Bias$ is the largest (0.47) in the most unstable case. This is because the AMPS overestimated the potential temperature gradient under an unstable atmosphere (see Fig. 6a, which will be discussed later). For the stable atmosphere, the lowest R_{xy} for $\log_{10}(Ri)$ seems to be consistent with the fact that model errors increase with increasing stability (Nigro et al., 2017).

190   Table 2 also shows an interesting result: the R_{xy} of $\log_{10}(Ri)$ is higher when the $RMSE$ of θ and V are smaller. Moreover, Hines et al. (2019) showed that using the Morrison microphysics scheme in the numerical model resulted in a smaller $RMSE$ for temperature and wind, than the default scheme (WSM5C) in AMPS. Therefore, we may conclude that replacing WSM5C with Morrison could improve the AMPS-forecasted $\log10(Ri)$. In other words, using Morrison may lead to higher R_{xy} for $\log10(Ri)$, as it simulates dynamic stability with less variability (the $RMSE$ for temperature and wind could be smaller). On

195   the other hand, larger $RMSE$ for θ and V are mainly found during cold months (JJA, SON), indicating that winter dynamic stability is more variable (similar to Bromwich et al., 2013).

     Table 2 summarises that the $\log_{10}(Ri)$ was overestimated by the AMPS at each site for every season (all $Bias$ are positive). This may be due to some local-scale dynamics not being represented properly (see Fig. 6, which will be discussed later). From another perspective, the model results were generally smoother than the measurements, and the atmosphere is less favorable

200   for the occurrence of turbulence under slowly changing meteorological parameters, then the AMPS-forecasted Ri could be larger.
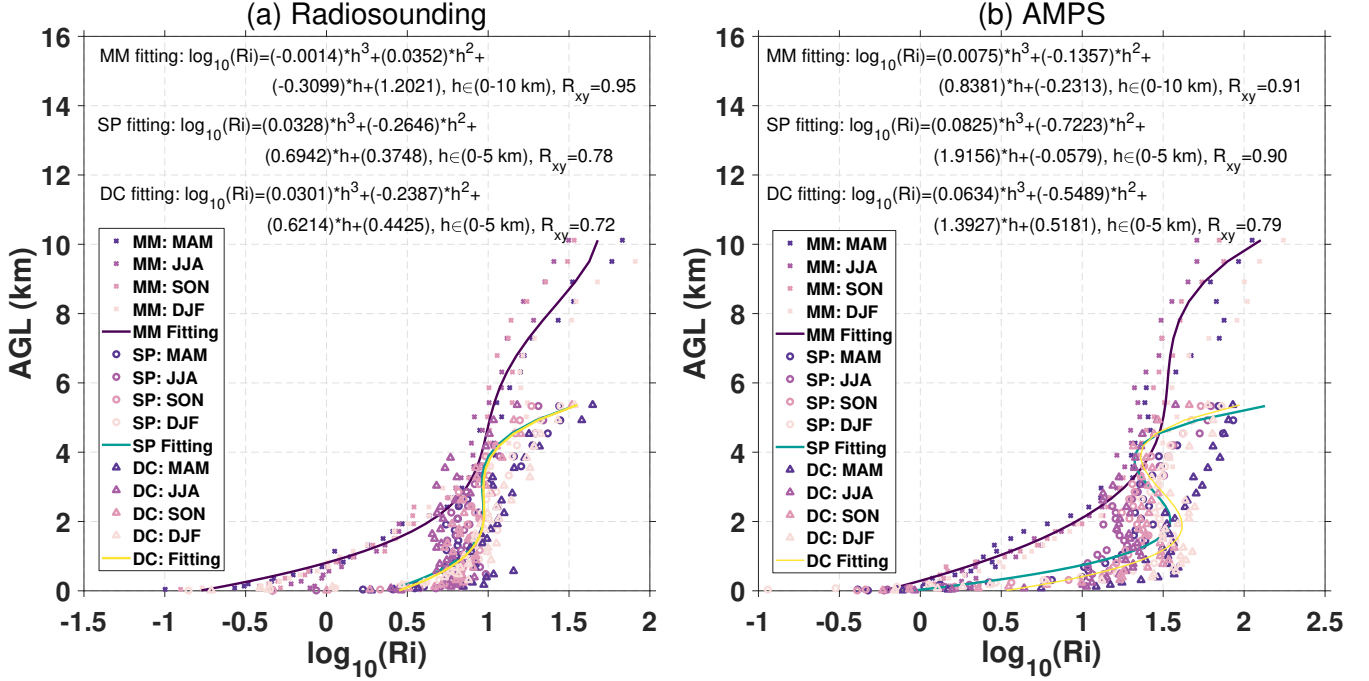
Figure 5. The polynomial curve fitting of near-ground median profiles of $\log_{10}(Ri)$ from Fig. 4. (a) the $\log_{10}(Ri)$ was estimated by the radiosonde measurements, (b) the $\log_{10}(Ri)$ was estimated by the AMPS forecasts.

The near-ground atmosphere in Antarctica is an important turbulence source, then an analytical function for $\log_{10}(Ri)$ profiles near the ground was fitted to better contextualize the results (as shown in Fig. 5). Fig. 5 shows that the near-ground $\log_{10}(Ri)$ profiles are the "C-C-C" shape. The "concave" structure in the "C-C-C" shape could be attributed by the near-ground
205   jet stream (Mihalikova et al., 2012). A cubic polynomial function was used (see the upper part of the plots in Fig. 5) instead of a logarithmic function, because the "C-C-C" shape seems hard for logarithmic function fitting. Moreover, each fitted curve used all four-seasons data points in Fig. 4, as the seasonal variation are not too significant. Nevertheless, one can see more details about the temporal variation of $\log_{10}(Ri)$ near the ground in Sect. 4.2.3.

Fig. 6 shows the AMPS performance under different potential temperature gradient ($G=\partial\theta/\partial z$) and wind shear ($S=$
210    $[(\partial u/\partial z)^2+(\partial v/\partial z)^2]^{1/2}$). The statistical results presented in Fig. 6 were counted based on all the collected data points at the three sites (MM, SP, and DC) for an entire year. One can see that the Ri was overestimated by the AMPS at unstable atmosphere (see light blue bin in Fig. 6a), where the AMPS has overestimated the potential temperature gradient (i.e. $\Delta G > 0$). But for strong temperature inversion (see dark red bin in Fig. 6a), the AMPS has underestimated the G and Ri. As for strong wind shear conditions (see dark red bin in Fig. 6b), when the Ri is small (basically corresponding to a near-surface layer with
215   a high probability of triggering strong turbulence, as in Fig. 4), the AMPS has underestimated the intensity of wind shear

($\Delta S < 0$). This may be caused by the AMPS has underestimated the wind speed near the ground (as in Fig. 3). In sum, if the model aims for a more accurate forecast of Ri, the biases under these atmospheric conditions need to be corrected.
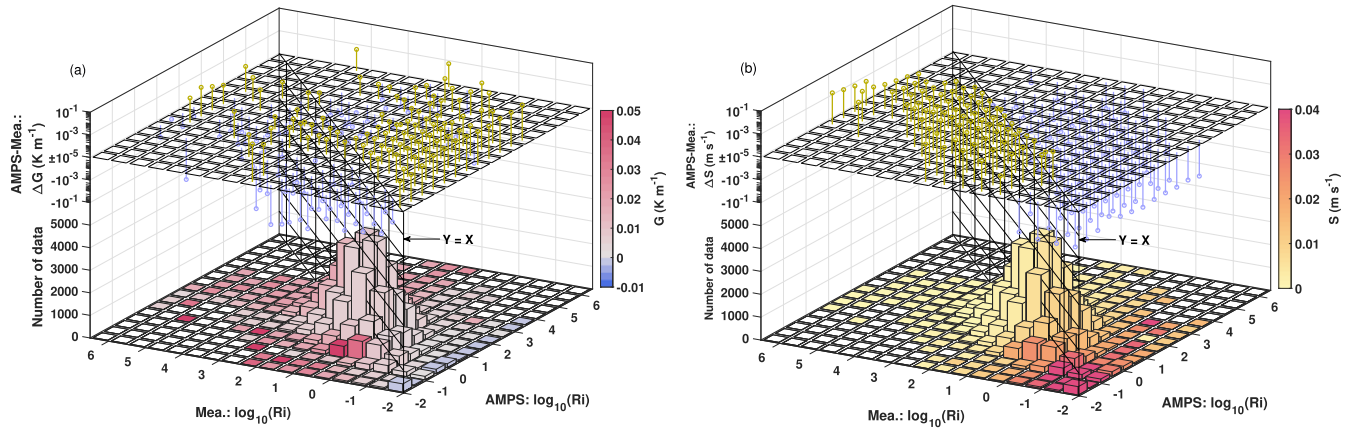
Figure 6. Performance of the AMPS under different atmospheric conditions. (a) and (b) are respectively the case of potential temperature gradient ($G=\partial\theta/\partial z$) and wind shear ($S = [(\partial u/\partial z\,)^2 + (\partial v/\partial z\,)^2]^{1/2}$). G (color of the bin in (a)), S (color of the bin in (b)), ΔG (stem above the bin in (a)) and ΔS (stem above the bin in (b)) are presented using the median value for each 0.5×0.5 bin of $\log_{10}(Ri)$.

4.2.2 Vertical cross-section

The results given in Sect. 4.2.1 show the AMPS can forecast the main tendency of $\log_{10}(Ri)$. Then, we consider that it is worth a try to use the AMPS-forecasted $\log_{10}(Ri)$ to comprehend the characteristics of atmospheric turbulence in Antarctica. The results of the AMPS-forecasted $\log_{10}(Ri)$ were presented through interpolation of the AMPS grid 2 field at two vertical cross-sections, which provides us with a broader perspective on the probability of turbulence triggered in four-dimensional space-time. One vertical cross-section is interpolated through the SP and DC, and another is through DA and MM, as shown in Fig. 7. The corresponding AMPS forecasts are shown in Figs. 8 and 9, respectively.

Figs. 8 and 9 show the seasonal median of the AMPS forecasts. The temperature and wind speed were lower above the Antarctic Plateau than over the ocean. In the polar winter (JJA), the temperature contours are dense near the ground above the interior Plateau, representing a strong surface-layer temperature inversion (such inversion has been observed by Yagüe et al., 2001; Argentini et al., 2013; Hu et al., 2019). The surface-layer wind speeds increase from the summit to the escarpment region (caused by the well-known katabatic wind over the surface slope area in Antarctica) and then decrease toward the coast, which is consistent with previous measurements (Ma et al., 2010; Rinke et al., 2012). The Ri is obviously larger above the summits (e.g. DA and DC), suggesting the $PBLH$ could be thin, this agrees with the results from Swain and Gallée (2006); Bonner et al. (2010); Aristidi et al. (2015).

The results of Ri distribution from the AMPS outputs provided us with valuable insights into the atmospheric turbulence in the Antarctic region, while using the radiosonde measurements is hard to do so. Here, we attempt to relate the features
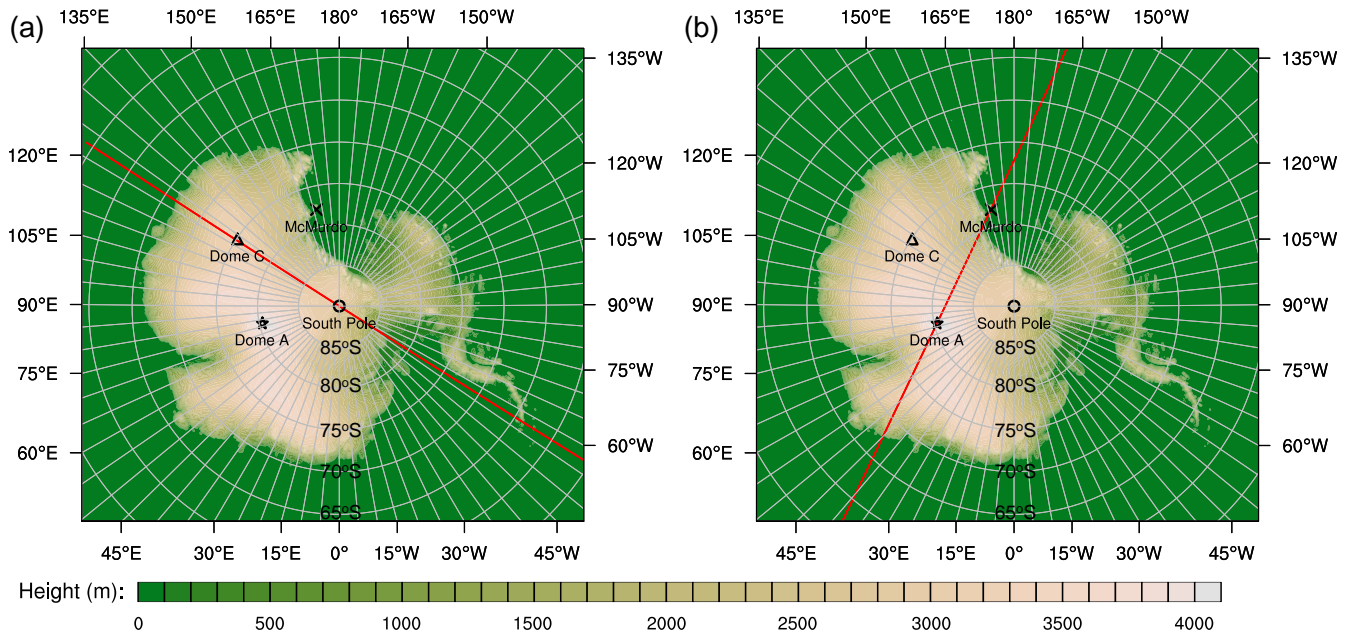
Figure 7. Two lines (marked by red lines) are used to create vertical cross-sections. (a) a line through DC and the SP, (b) a line through DA and MM. The color scale indicates the terrain height (m), where terrain fields are generated from the RAMP2 data set (https://nsidc.org/data/nsidc-0082/versions/2).

of atmospheric turbulence to some large-scale phenomena or local-scale dynamics over the Antarctic plateau and the ocean surrounding it: the shear-induced turbulence (katabatic winds, polar vortices), convection (cloud cooling, boundary layer convection), temperature inversion, and the wave-induced turbulence (orographic gravity waves, trapped lee waves, inertia-gravity waves). Table 3 lists their possible functional areas that are marked in Figs. 8 and 9. This is dedicated to qualitatively evaluating the AMPS outputs and investigating the underlying physical processes of triggering atmospheric turbulence.

As a result of katabatic winds (Rinke et al., 2012), the near-surface wind speeds increase from the interior plateau to the steep slope (Figs. 8 and 9), which is driven by gravity. Strong winds can lead to strong wind shear and increased levels of mechanical turbulence (e.g., Huang et al., 2021; Solanki et al., 2022), as one can see the surface layer with small Ri at the escarpment region (see A8 and A11 areas in Fig. 8, B3 and B5 areas in Fig. 9). Where the regions between the SP and DC (in A8 area) are also located on the slope (see Fig. 7a) and show a relatively small Ri near the ground.

A strong polar vortex implies that the zonal winds are intense, and atmospheric turbulence is more prone to occur. The Antarctic polar vortex reaches its maximum intensity in the winter-spring season (Zuev and Savelieva, 2019a), which corresponds to the relatively turbulent free atmosphere with low Ri values over the ocean during JJA and SON (see Figs. 8 and 9). Moreover, the strongest zonal winds are located over the ocean (Zuev and Savelieva, 2019b), the interaction between the zonal wind and the ocean surface may generate wind shear and facilitate the development of turbulence (see areas A2 and A12 in Fig. 8, B2 and B9 in Fig. 9).
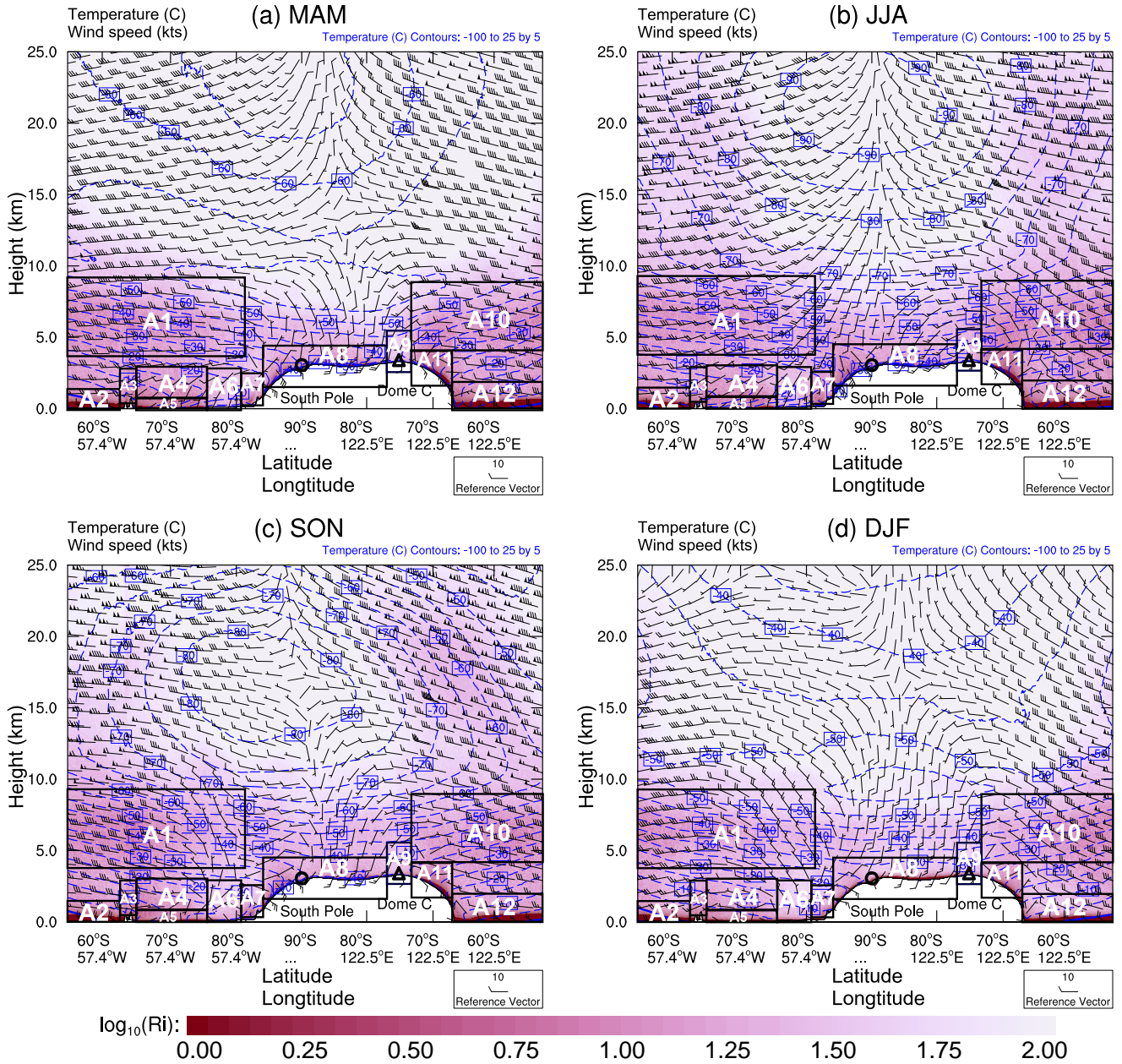
Figure 8. The seasonal median of temperature, wind speed, and $\log_{10}(Ri)$ along the vertical cross-section through the South Pole (black circle) and Dome C (black triangle), as shown by the red line in Fig. 7a. The height (km) on the y-axis represents the elevation above sea level. The AX in each plot are used to mark the possible functional areas of some atmospheric activities (as listed in Table 3).

Cloud cooling refers to two kinds of cooling-induced turbulence in this study: Cloud Top Cooling (CTC) and Below Cloud-base Turbulence (BCT). The CTC is contributed by radiative cooling, which could be one of the driving mechanisms of
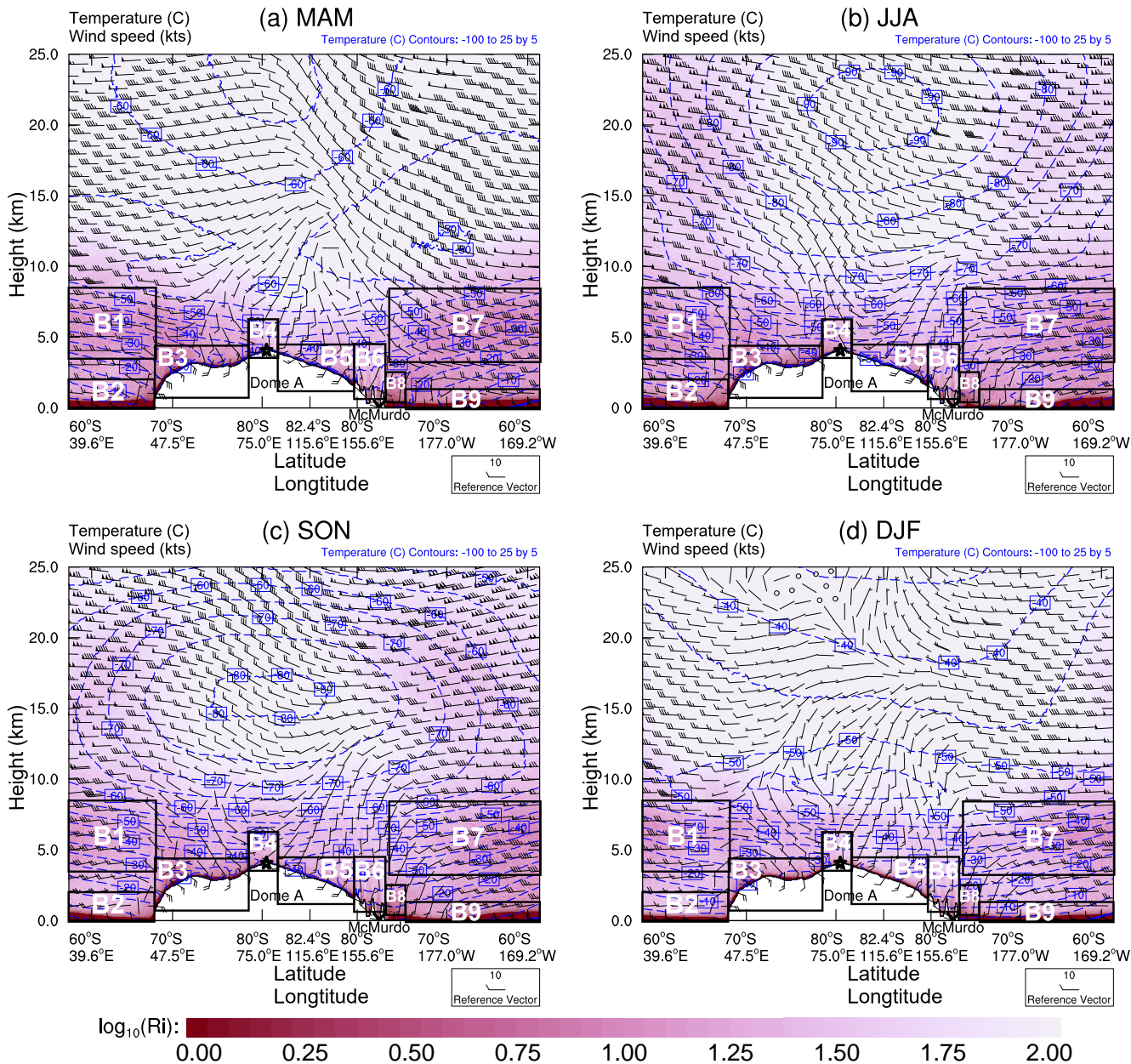
Figure 9. As in Fig. 8, but for the vertical cross-section through Dome A (black star) and McMurdo (black cross), as shown by the red line in Fig. 7b.

the mixed-layer turbulence (Deardorff, 1976). The BCT usually occurs below the bases of midlevel clouds accompanied by precipitation that does not reach the ground, cooling by evaporation or sublimation seems to contribute to the turbulence (Kudo, 2013; Kantha et al., 2019). In sum, regions with clouds may advance the development of turbulence. The cloud fraction

Table 3. The possible functional areas of some typical large-scale phenomena or local-scale dynamics over the Antarctic plateau and the ocean surrounding it.

| Atmospheric activities | Possible functional areas | | Contribution for triggering turbulence |
	Marked areas in Fig. 8	Marked areas in Fig. 9	
Katabatic winds	A8, A11	B3, B5	Positive
Polar vortices	A1, A2, A5, A10, A12	B1, B2, B7, B9	Positive
Cloud cooling	A1, A10	B1, B7	Positive
Boundary layer convection	A2, A5, A12	B2, B9	Positive
Temperature inversion	A6, A9	B4	Negative
Orographic gravity waves	A3	B6	Positive
Trapped lee waves	A4, A7	B8	Positive
Inertia-gravity waves	A1, A10	B1, B7	Positive

observed by satellite lidar is higher above the ocean than the Antarctic plateau (Spinhirne et al., 2005; Saunders et al., 2009). Thus, cloud may benfit small Ri above the ocean (A1 and A10 areas in Fig. 8, plus the B1 and B7 areas in Fig. 9).

Boundary layer convection is generated by forcing from the ground, solar heating of the ground during sunny days causes thermals of warmer air to rise and convection will form (He et al., 2020), then the turbulence could be developed forced by
260 buoyancy (Verma et al., 2017). The albedo of fresh snow over sea ice is very high, while that for open water is relatively small (Hines et al., 2015). Thus, solar heating will be much more stand out over open water and lead to the thermal convection boom. This can be used to reasonably explain the results in Fig. 8, that the Ri over ocean (A2 area) is smaller than over ice shelf (A6 area), and the A5 area can be regarded as a "transition region" (sea ice and open water could both exist) between them with an intermediate value of Ri.

265 The strength of the near-ground temperature inversion forecasted by the AMPS increases from the coast to the high interior, and its strength weakens during polar summer, such a phenomenon has also been observed in previous studies (Hudson and Brandt, 2005; Ma et al., 2010). The general increase in temperature-inversion strength was considered to correspond to a less turbulent atmosphere when the boundary layer is shallower, owing to large stability suppressing turbulence. This corresponds to the larger Ri in the summit area where a stronger temperature inversion occurred (see A9 area in Fig. 8 and B4 area in
270 Fig. 9). There is a similar phenomenon occurred over the Ronne ice shelf (A6 area in Fig. 8), especially for JJA when the temperature inversion is more obvious. Importantly, it should be noted that it is the range of turbulence (or $PBLH$) that would be suppressed by the temperature inversion and the turbulence intensity could be strong within the inversion layer (Petenko et al., 2019). For example, the turbulence above Dome C is mainly concentrated in the first tens of meters above the ground (Aristidi et al., 2015).

275 The development of Orographic Gravity Wave (OGW) is the interaction between near-surface wind and a mountain barrier (Lv et al., 2021; Zhang et al., 2022a, b), the OGW breaking could be a source of turbulence. Obviously, OGW can be triggered

above the Antarctic Peninsula (A3 area in Fig. 8) and Transantarctic Mountains (B6 area in Fig. 9). But the atmosphere just above the top of the mountain seems to be laminar (e.g., see the larger value of Ri in B6 area), this may be due to that the breaking of the OGW may not happen immediately after being generated above the mountains.

280   Trapped Lee Waves (TLW) belongs to OGW. Specially, TLW, as its name implies, tends to form on the lee side of mountains and turbulence may be developed in the downstream (Xue et al., 2022). Thus, the small Ri in A4 area in Fig. 8 can be attributed by the TLW forced by the Antarctic Peninsula (see its position in Fig. 7a). It is the same case for B8 area in Fig. 9 (but forced by the Transantarctic Mountains). The katabatic winds could be linked to TLW and result in enhanced turbulence, This could explain the A7 area (Fig. 8) have small Ri on the lee side of the mountain.

285   Inertia-Gravity Waves (IGW) are influenced by the Coriolis effect (increasing with wind speed), and the frequency of IGW is close to inertial frequency. IGW and Kelvin-Helmholtz instability (which can be characterized by the Ri) are generally presumed to be closely linked. At high latitudes, the IGW energy density's maxima occur at around 5 km AGL (Zhang et al., 2022b). This may suggest that the IGW can also be a contributor to the small Ri above the ocean (A1 and A10 areas in Fig. 8, plus the B1 and B7 areas in Fig. 9).

290   In addition, one can see the temporal evolution of Ri vertical cross-sections for a year from the video supplement (vertical cross-section through the red line shown in Fig. 7a: https://doi.org/10.5446/60761 and Fig. 7b: https://doi.org/10.5446/60760). It shows that the atmospheric conditions are variable, and a significant transition between laminar flow and turbulent flow could occur at any time. Some activities in Antarctica require a non-turbulent atmosphere, such as astronomical observations (Burton, 2010) and aviation safety (Gultepe and Feltz, 2019). Therefore, real-time forecasting of the Ri is important and helpful, rather

295   than relying solely on the statistical results presented in this study. Furthermore, the video shows that atmospheric turbulence is likely to be triggered over the ocean, moving toward the Antarctic Plateau and weakening. This may be due to the obstruction of the high plateau, which creates a calm atmosphere above it.

4.2.3   Richardson number at the planetary boundary layer height

The Ri is used to determine the $PBLH$ using a critical value (Troen and Mahrt, 1986; Holtslag et al., 1990; Pietroni et al.,

300   2012). Thus, the critical value (or the value of Ri at the $PBLH$, Ri_{PBLH}) is worth studying. In addition, previous studies have suggested that the Ri_{PBLH} depends on the vertical resolution of the data (Troen and Mahrt, 1986; Holtslag et al., 1990). As for the resolution of the AMPS grid, it is necessary to recalculate Ri_{PBLH} based on the AMPS outputs, since the value of Ri_{PBLH} is a helpful reference for judging whether atmospheric turbulence is likely to be suppressed ($Ri > Ri_{PBLH}$) or developed ($Ri < Ri_{PBLH}$).

305   The planetary boundary layer scheme of Polar WRF in the AMPS was the Mellor-Yamada-Janjić (Janjić, 1994) scheme, and the ability of the AMPS to model the Antarctic boundary layer has been examined by (Wille et al., 2017). The MYJ scheme defines the $PBLH$ where turbulent kinetic energy decreases to a prescribed value of 0.1 $\mathrm{m^2 s^{-2}}$ (Xie et al., 2012). The AMPS forecasts include the values of $PBLH$. Figs. 10a and 11b show that the $PBLH$ directly forecasted by the AMPS was mostly less than 100 m in the summit (DC and DA) during the polar winter, such variation range is consistent with the SODAR

310   observations (DC: Petenko et al., 2014; DA: Bonner et al., 2010); Fig. 10b also displays a result being in accordance with the
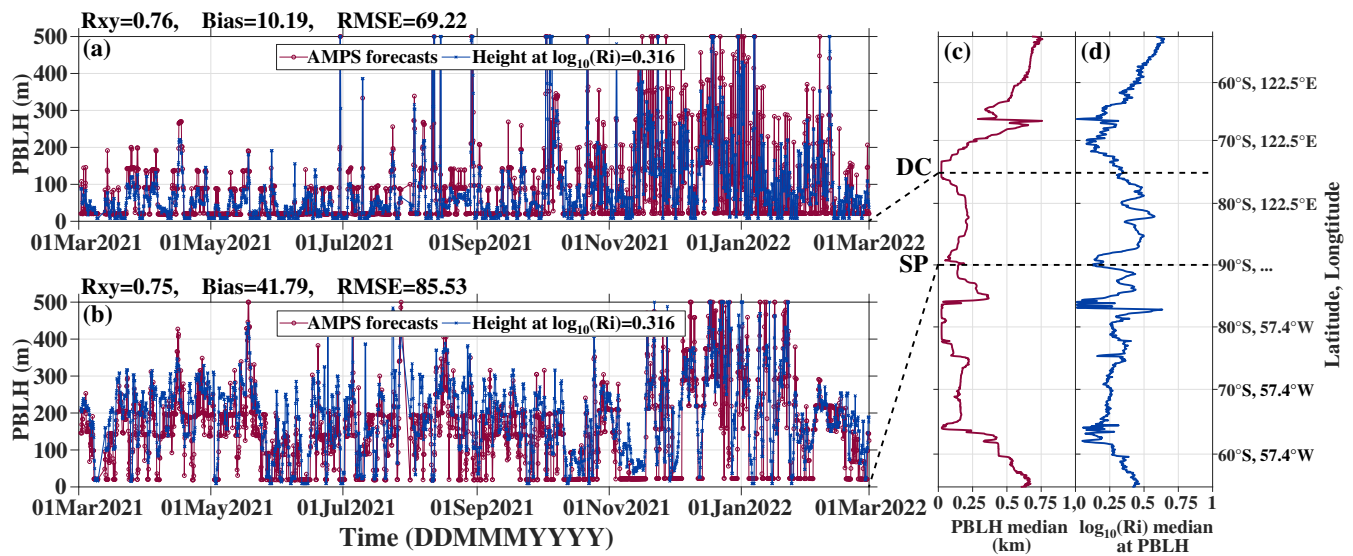
Figure 10. Temporal evolution of $PBLH$ directly forecasted by the AMPS (red circles) and estimated by the height corresponding to $\log_{10}(Ri)$=0.316 (blue crosses) at DC (a) and SP (b). Median annual $PBLH$ (c) and $\log_{10}(Ri)$ at the $PBLH$ (d) along the red line through DC and SP shown in Fig. 7a.
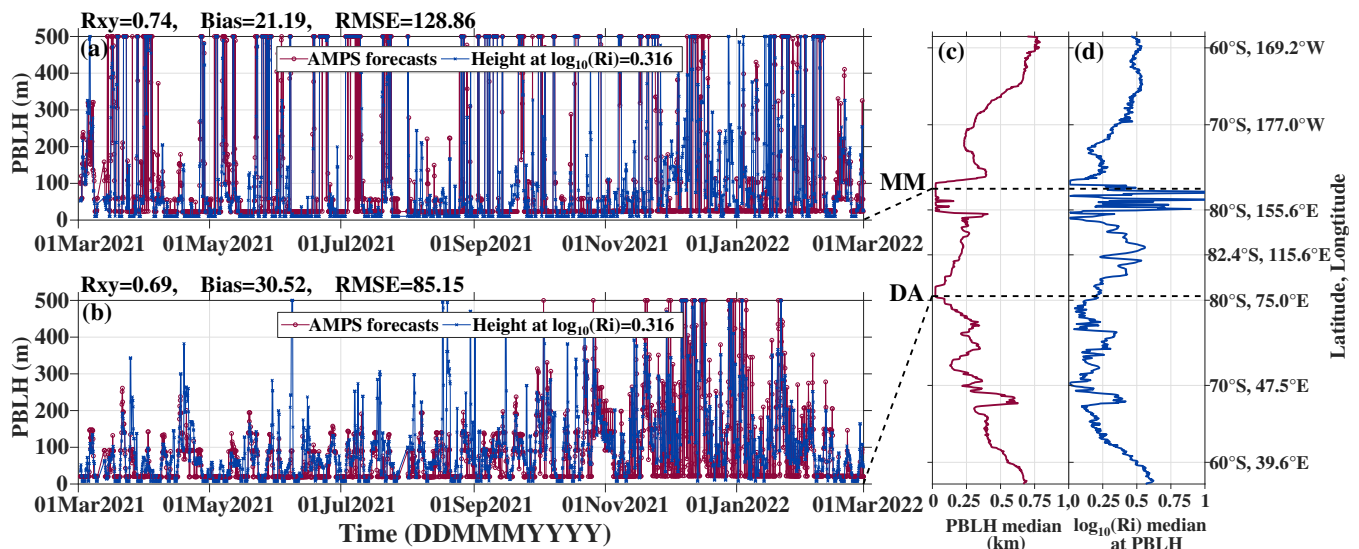
Figure 11. As in Fig. 10, but for data above MM and DA, plus the red line through MM and DA shown in Fig. 7b.

SODAR observations at the SP, as the most $PBLH$ was shown to be within 100-300 m (Travouillon et al., 2003). Thus, the AMPS-forecasted $PBLH$ is considered to be realistic.

Figs. 10c and 11c show the median annual $PBLH$ forecasted by AMPS along the red lines in Figs. 7a and 7b, respectively. A thin $PBLH$ over the plateau can be observed, especially at the Domes (e.g., DA and DC), which is consistent with previous studies (Swain and Gallée, 2006). In contrast, a thick $PBLH$ is shown near the escarpment region, e.g., ∼68°S, 122.5°E in Fig. 10c; this corresponds to the relatively low Ri near the ground in A11 area in Fig. 8.

The $\log_{10}(Ri_{PBLH})$ was computed using linear interpolation between the grid with height equals to the AMPS-forecasted $PBLH$. The median value of $\log_{10}(Ri_{PBLH})$ from the combined data of two vertical cross-sections (i.e. Figs. 10d and 11d) was calculated as 0.316, i.e., median $\log_{10}(Ri_{PBLH})$ equals to 0.316 (or Ri_{PBLH}=2.07). However, some researchers have employed Ri_{PBLH}=0.25 when the radiosonde measurements with a higher vertical resolution was used (e.g. at Dome C; Pietroni et al., 2012). Here, the larger Ri_{PBLH} for the AMPS forecasts may be caused by the coarse vertical grid resolution (as implied from Troen and Mahrt, 1986) and its data smoothness (as mentioned in Sect. 4.2.1; the AMPS forecasts show larger Ri than the radiosoundings even though they have already been interpolated to the same vertical grid).

To test the credibility of the critical value (i.e. $\log_{10}(Ri_{PBLH})$=0.316), $PBLH$ was also derived as the height where the AMPS-forecasted $\log_{10}(Ri)$ decreases to 0.316. The R_{xy}, $Bias$, and $RMSE$ of $PBLH$ between the estimations using the critical value (blue lines in Figs. 10a-b and 11a-b) and the direct forecasts of AMPS (red lines in Figs. 10a-b and 11a-b) are depicted in the top left of the plot, where $Bias$ indicates the former minus the latter. It appears that the values of R_{xy} (all larger than 0.69) are almost satisfactory, then we may conclude that $\log_{10}(Ri_{PBLH})$=0.316 is a reliable critical value for judging the behavior of atmospheric turbulence. The atmosphere layer could be considered turbulent for $\log_{10}(Ri_{PBLH})$<0.316 and the turbulence intensity could be comparable to that within the boundary layer. However, this critical value may only be valid for using the AMPS forecasts.

5   Conclusions

We have examined the ability of AMPS to forecast the atmospheric Ri in the Antarctic atmosphere. This includes evaluating the accuracy of meteorological parameters (θ and V, on which the Ri depends), and comparing the $\log_{10}(Ri)$ estimations between radiosoundings and AMPS forecasts. In addition, the analysis of atmospheric $\log_{10}(Ri)$ over the entire Antarctic continent and the ocean surrounding it, was presented on an annual time scale. Finally, the $\log_{10}(Ri)$ at the $PBLH$ has been calculated.

From the analysis presented above, we deduce the following:

1. Comparisons of AMPS forecasts with radiosoundings from three representative sites (coast: McMurdo, flank: South Pole, summit: Dome C) show that the forecasts can accurately describe the trend of atmospheric meteorological parameters above the Antarctic continent, as the R_{xy} for θ reached as high as 0.99 and the R_{xy} for V are all larger than 0.85 (Table 2).

2. We proved that the AMPS forecasts can identify the main characteristics of atmospheric turbulence over the Antarctic continent in terms of both space and time. The R_{xy} of $\log_{10}(Ri)$ at MM, SP, and DC are 0.71, 0.59, and 0.53, respectively. And the AMPS can reconstruct the near-ground "convex-concave–convex" shaped $\log_{10}(Ri)$ profiles indicated by the radiosonde measurements (Fig. 5). We also find that the R_{xy} of $\log_{10}(Ri)$ would be higher when the $RMSE$ of θ and V are smaller

(Table 2). Besides, the AMPS can better capture the trend of $\log_{10}(Ri)$ (R_{xy} would be larger) at a relatively unstable atmosphere (weaker temperature inversion). Moreover, the values of $\log_{10}(Ri)$ were generally overestimated at the three sites; this is partly the result of the potential temperature gradients at the unstable atmosphere being overestimated by the AMPS, and the AMPS has generally underestimated the wind shear when it was strong.

350   3. The seasonal medians of the AMPS forecasts from two vertical cross-sections were presented (Figs. 8 and 9). which provides us with a broader perspective on when and where atmospheric turbulence could be highly triggered in the Antarctic region. The AMPS-forecasted $\log_{10}(Ri)$ were qualitatively verified, as its statistical distribution behaved as the expected atmospheric properties attributed by some typical large-scale phenomena or local-scale dynamics (katabatic winds, polar vortices, convection, gravity wave, etc.) over the Antarctic plateau and the ocean surrounding it. For example, a very laminar atmosphere
355 above the Antarctic Plateau and a shallow boundary layer in the Domes area are illustrated by the AMPS forecasts.

4. The $\log_{10}(Ri)$ at the $PBLH$ were calculated and their median value is 0.316, $\log_{10}(Ri)$=0.316 in turn was used to calculate $PBLH$ and agree well with the AMPS-forecasted $PBLH$ (R_{xy}> 0.69). The atmosphere layer could be considered turbulent at $\log_{10}(Ri)$<0.316 and the turbulence intensity could be comparable to that within the boundary layer.

The overall results show that the AMPS can forecast a realistic behaviour of Ri, and the turbulence conditions in Antarctica
360 are well revealed; furthermore, some practical operations that want to avoid a turbulent atmosphere — such as astronomical observations (Burton, 2010), aviation safety (Gultepe and Feltz, 2019), and free space optical communication (Yin et al., 2017) — can apply the AMPS-forecasted Ri.

Data availability. The meteorological parameters measured by the radiosondes at McMurdo, South Pole that support the findings of this study are available at the Antarctic Meteorological Research Center (ftp://amrc.ssec.wisc.edu/pub), while the meteorological parameters at
365 Dome C are available at the Antarctic Meteo-Climatological Observatory (http://www.climantartide.it). The original WRF output files of AMPS used in this study can be found at https://www2.mmm.ucar.edu/rt/amps/information/amps_esg_data_info.html.

Video supplement. The annual AMPS forecasts change related to the vertical cross-section through the South Pole and Dome C (Fig. 7a) is available online at https://doi.org/10.5446/60761. Another vertical cross-section through Dome A and McMurdo (Fig. 7b) is https://doi.org/10.5446/60760.

370 *Author contributions.* QY and XW planned the investigation; QY, XH, XW, and ZW analyzed the data; QY and YG wrote the manuscript draft; QY finished the visualizition; QY, XW, XH, XQ, and ZW performed the valiation; XW, CQ, TL, XQ, and PW reviewed and edited the manuscript.

Competing interests. The authors declare that they have no conflict of interest.

Acknowledgements. This work was supported by the National Natural Science Foundation of China (grant Nos. 91752103, 41576185), Foundation of Key Laboratory of Science and Technology Innovation of Chinese Academy of Sciences (grant No. CXJJ-21S028) and the Foundation of Advanced Laser Technology Laboratory of Anhui Province (grant No. AHL2021QN02).

375

References

Agabi, A., Aristidi, E., Azouit, M., Fossat, E., Martin, F., Sadibekova, T., Vernin, J., and Ziad, A.: First Whole Atmosphere Nighttime Seeing Measurements at Dome C, Antarctica, Publications of the Astronomical Society of the Pacific, 118, 344–348, https://doi.org/10.1086/498728, 2006.

Argentini, S., Pietroni, I., Mastrantonio, G., Viola, A. P., Dargaud, G., and Petenko, I.: Observations of near surface wind speed, temperature and radiative budget at Dome C, Antarctic Plateau during 2005, Antarctic Science, 26, 104–112, https://doi.org/10.1017/s0954102013000382, 2013.

Aristidi, E., Agabi, K., Azouit, M., Fossat, E., Vernin, J., Travouillon, T., Lawrence, J. S., Meyer, C., Storey, J. W. V., Halter, B., Roth, W. L., and Walden, V.: An analysis of temperatures and wind speeds above Dome C, Antarctica, Astronomy and Astrophysics, 430, 739–746, https://doi.org/10.1051/0004-6361:20041876, 2005.

Aristidi, E., Vernin, J., Fossat, E., Schmider, F. X., Travouillon, T., Pouzenc, C., Traullé, O., Genthon, C., Agabi, A., Bondoux, E., Challita, Z., Mékarnia, D., Jeanneaux, F., and Bouchez, G.: Monitoring the optical turbulence in the surface layer at Dome C, Antarctica, with sonic anemometers, Monthly Notices of the Royal Astronomical Society, 454, 4304–4315, https://doi.org/10.1093/mnras/stv2273, 2015.

Bonner, C. S., Ashley, M. C. B., Cui, X., Feng, L., Gong, X., Lawrence, J. S., Luong-Van, D. M., Shang, Z., Storey, J. W. V., Wang, L., Yang, H., Yang, J., Zhou, X., and Zhu, Z.: Thickness of the Atmospheric Boundary Layer Above Dome A, Antarctica, during 2009, Publications of the Astronomical Society of the Pacific, 122, 1122–1131, https://doi.org/10.1086/656250, 2010.

Boville, B. A., Kiehl, J. T., and Briegleb, B. P.: Evolution of the Antarctic polar vortex in spring: Response of a GCM to a prescribed Antarctic ozone hole, Report, NASA, Goddard Space Flight Center, Polar Ozone Workshop., https://doi.org/https://ntrs.nasa.gov/citations/19890005218, 1988.

Bromwich, D. H., Otieno, F. O., Hines, K. M., Manning, K. W., and Shilo, E.: Comprehensive evaluation of polar weather research and forecasting model performance in the Antarctic, Journal of Geophysical Research: Atmospheres, 118, 274–292, https://doi.org/10.1029/2012jd018139, 2013.

Burton, M. G.: Astronomy in Antarctica, Astron. Astrophys. Rev., 18, 417–469, https://doi.org/10.1007/s00159-010-0032-2, 2010.

Chan, P. W.: Determination of Richardson number profile from remote sensing data and its aviation application, IOP Conference Series: Earth and Environmental Science 1, 012043, https://doi.org/10.1088/1755-1307/1/1/012043, 2008.

Deardorff, J. W.: On the entrainment rate of a stratocumulus-topped mixed layer, Quarterly Journal of the Royal Meteorological Society, 102, 563–582, https://doi.org/10.1002/qj.49710243306, 1976.

Gallée, H., Preunkert, S., Argentini, S., Frey, M. M., Genthon, C., Jourdain, B., Pietroni, I., Casasanta, G., Barral, H., Vignon, E., Amory, C., and Legrand, M.: Characterization of the boundary layer at Dome C (East Antarctica) during the OPALE summer campaign, Atmos. Chem. Phys., 15, 6225–6236, https://doi.org/10.5194/acp-15-6225-2015, 2015.

Geissler, K. and Masciadri, E.: Meteorological Parameter Analysis above Dome C Using Data from the European Centre for Medium-Range Weather Forecasts, Publications of the Astronomical Society of the Pacific, 118, 1048–1065, https://doi.org/10.1086/505891, 2006.

Gultepe, I. and Feltz, W. F.: Aviation Meteorology: Observations and Models. Introduction, Pure and Applied Geophysics, 176, 1863–1867, https://doi.org/10.1007/s00024-019-02188-2, 2019.

Hagelin, S., Masciadri, E., Lascaux, F., and Stoesz, J.: Comparison of the atmosphere above the South Pole, Dome C and Dome A: first attempt, Monthly Notices of the Royal Astronomical Society, 387, 1499–1510, https://doi.org/10.1111/j.1365-2966.2008.13361.x, 2008.

Han, Y., Yang, Q., Liu, N., Zhang, K., Qing, C., Li, X., Wu, X., and Luo, T.: Analysis of wind-speed profiles and optical turbulence above Gaomeigu and the Tibetan Plateau using ERA5 data, Monthly Notices of the Royal Astronomical Society, 501, 4692–4702,

415   https://doi.org/10.1093/mnras/staa2960, 2021.

He, Y., Sheng, Z., and He, M.: The First Observation of Turbulence in Northwestern China by a Near-Space High-Resolution Balloon Sensor, Sensors, 20, 677, https://doi.org/10.3390/s20030677, 2020.

Hines, K. M. and Bromwich, D. H.: Development and Testing of Polar Weather Research and Forecasting (WRF) Model. Part I: Greenland Ice Sheet Meteorology*, Monthly Weather Review, 136, 1971–1989, https://doi.org/10.1175/2007mwr2112.1, 2008.

420   Hines, K. M., Bromwich, D. H., Bai, L., Bitz, C. M., Powers, J. G., and Manning, K. W.: Sea Ice Enhancements to Polar WRF*, Monthly Weather Review, 143, 2363–2385, https://doi.org/10.1175/mwr-d-14-00344.1, 2015.

Hines, K. M., Bromwich, D. H., Wang, S.-H., Silber, I., Verlinde, J., and Lubin, D.: Microphysics of summer clouds in central West Antarctica simulated by the Polar Weather Research and Forecasting Model (WRF) and the Antarctic Mesoscale Prediction System (AMPS), Atmospheric Chemistry and Physics, 19, 12 431–12 454, https://doi.org/10.5194/acp-19-12431-2019, 2019.

425   Holtslag, A. A. M., de Bruijn, E. I. F., and Pan, H. L.: A High Resolution Air Mass Transformation Model for Short-Range Weather Forecasting, Monthly Weather Review, 118, 1561, https://doi.org/10.1175/1520-0493(1990)118<1561:Ahramt>2.0.Co;2, 1990.

Hu, Y., Hu, K., Shang, Z., Ashley, M. C. B., Ma, B., Du, F., Li, Z., Liu, Q., Wang, W., Yang, S., Yu, C., and Zeng, Z.: Meteorological Data from KLAWS-2G for an Astronomical Site Survey of Dome A, Antarctica, Publications of the Astronomical Society of the Pacific, 131, 015 001, https://doi.org/10.1088/1538-3873/aae916, 2019.

430   Huang, T., Yang, Y., O'Connor, E. J., Lolli, S., Haywood, J., Osborne, M., Cheng, J. C.-H., Guo, J., and Yim, S. H.-L.: Influence of a weak typhoon on the vertical distribution of air pollution in Hong Kong: A perspective from a Doppler LiDAR network, Environmental Pollution, 276, 116 534, https://doi.org/10.1016/j.envpol.2021.116534, 2021.

Hudson, S. R. and Brandt, R. E.: A Look at the Surface-Based Temperature Inversion on the Antarctic Plateau, Journal of Climate, 18, 1673–1696, https://doi.org/10.1175/jcli3360.1, 2005.

435   Janjić, Z. I.: The Step-Mountain Eta Coordinate Model: Further Developments of the Convection, Viscous Sublayer, and Turbulence Closure Schemes, Monthly Weather Review, 122, 927–945, https://doi.org/10.1175/1520-0493(1994)122<0927:Tsmecm>2.0.Co;2, 1994.

Kantha, L., Luce, H., and Hashiguchi, H.: Midlevel Cloud-Base Turbulence: Radar Observations and Models, Journal of Geophysical Research: Atmospheres, 124, 3223–3245, https://doi.org/10.1029/2018JD029479, 2019.

Karpetchko, A., Kyrö, E., and Knudsen, B. M.: Arctic and Antarctic polar vortices 1957–2002 as seen from the ERA-40 reanalyses, Journal

440   of Geophysical Research, 110, https://doi.org/10.1029/2005jd006113, 2005.

Kudo, A.: The Generation of Turbulence below Midlevel Cloud Bases: The Effect of Cooling due to Sublimation of Snow, Journal of Applied Meteorology and Climatology, 52, 819–833, https://doi.org/10.1175/jamc-d-12-0232.1, 2013.

Lascaux, F., Masciadri, E., Hagelin, S., and Stoesz, J.: Mesoscale optical turbulence simulations at Dome C, Monthly Notices of the Royal Astronomical Society, 398, 1093–1104, https://doi.org/10.1111/j.1365-2966.2009.15151.x, 2009.

445   Listowski, C. and Lachlan-Cope, T.: The microphysics of clouds over the Antarctic Peninsula – Part 2: modelling aspects within Polar WRF, Atmospheric Chemistry and Physics, 17, 10 195–10 221, https://doi.org/10.5194/acp-17-10195-2017, 2017.

Lv, Y., Guo, J., Li, J., Cao, L., Chen, T., Wang, D., Chen, D., Han, Y., Guo, X., Xu, H., Liu, L., Solanki, R., and Huang, G.: Spatiotemporal characteristics of atmospheric turbulence over China estimated using operational high-resolution soundings, Environmental Research Letters, 16, 054 050, https://doi.org/10.1088/1748-9326/abf461, 2021.

450   Ma, B., Shang, Z., Hu, Y., Hu, K., Wang, Y., Yang, X., Ashley, M. C. B., Hickson, P., and Jiang, P.: Night-time measurements of astronomical seeing at Dome A in Antarctica, Nature, 583, 771–774, https://doi.org/10.1038/s41586-020-2489-0, 2020.

Ma, Y., Bian, L., Xiao, C., Allison, I., and Zhou, X.: Near surface climate of the traverse route from Zhongshan Station to Dome A, East Antarctica, Antarctic Science, 22, 443–459, https://doi.org/10.1017/s0954102010000209, 2010.

Marks, R. D., Vernin, J., Azouit, M., Manigault, J. F., and Clevelin, C.: Measurement of optical seeing on the high antarctic plateau, Astronomy and Astrophysics Supplement Series, 134, 161–172, https://doi.org/10.1051/aas:1999100, 1999.

Mihalikova, M., Kirkwood, S., Arnault, J., and Mikhaylova, D.: Observation of a tropopause fold by MARA VHF wind-profiler radar and ozonesonde at Wasa, Antarctica: comparison with ECMWF analysis and a WRF model simulation, Ann. Geophys., 30, 1411–1421, https://doi.org/10.5194/angeo-30-1411-2012, 2012.

Monaghan, A. J., Bromwich, D. H., Powers, J. G., and Manning, K. W.: The Climate of the McMurdo, Antarctica, Region as 460   Represented by One Year of Forecasts from the Antarctic Mesoscale Prediction System, Journal of Climate, 18, 1174–1189, https://doi.org/10.1175/JCLI3336.1, 2005.

Nigro, M. A., Cassano, J. J., Wille, J., Bromwich, D. H., and Lazzara, M. A.: A Self-Organizing-Map-Based Evaluation of the Antarctic Mesoscale Prediction System Using Observations from a 30-m Instrumented Tower on the Ross Ice Shelf, Antarctica, Weather and Forecasting, 32, 223–242, https://doi.org/10.1175/waf-d-16-0084.1, 2017.

465   P. Lönnberg, D. S.: ECMWF Data Assimilation - scientific documentation, 3rd ed., Report, https://www.ecmwf.int/en/elibrary/75427-ecmwf-data-assimilation-scientific-documentation-3rd-ed, 1992.

Petenko, I., Argentini, S., Pietroni, I., Viola, A., Mastrantonio, G., Casasanta, G., Aristidi, E., Bouchez, G., Agabi, A., and Bondoux, E.: Observations of optically active turbulence in the planetary boundary layer by sodar at the Concordia astronomical observatory, Dome C, Antarctica, Astronomy and Astrophysics, 568, https://doi.org/10.1051/0004-6361/201323299, 2014.

470   Petenko, I., Argentini, S., Casasanta, G., Genthon, C., and Kallistratova, M.: Stable Surface-Based Turbulent Layer During the Polar Winter at Dome C, Antarctica: Sodar and In Situ Observations, Boundary-Layer Meteorology, 171, 101–128, https://doi.org/10.1007/s10546-018-0419-6, 2019.

Pietroni, I., Argentini, S., Petenko, I., and Sozzi, R.: Measurements and Parametrizations of the Atmospheric Boundary-Layer Height at Dome C, Antarctica, Boundary-Layer Meteorology, 143, 189–206, https://doi.org/10.1007/s10546-011-9675-4, 2012.

475   Powers, J. G., Manning, K. W., Bromwich, D. H., Cassano, J. J., and Cayette, A. M.: A Decade of Antarctic Science Support Through Amps, Bulletin of the American Meteorological Society, 93, 1699–1712, https://doi.org/10.1175/BAMS-D-11-00186.1, 2012.

Richardson, L. F. and Shaw, W. N.: The supply of energy from and to atmospheric eddies, Proceedings of the Royal Society of London. Series A, Containing Papers of a Mathematical and Physical Character, 97, 354–373, https://doi.org/10.1098/rspa.1920.0039, 1920.

Rinke, A., Ma, Y., Bian, L., Xin, Y., Dethloff, K., Persson, P. O. G., Lüpkes, C., and Xiao, C.: Evaluation of atmospheric boundary layer-480   surface process relationships in a regional climate model along an East Antarctic traverse, Journal of Geophysical Research: Atmospheres, 117, n/a–n/a, https://doi.org/10.1029/2011jd016441, 2012.

Saunders, W., Lawrence, J. S., Storey, J. W. V., Ashley, M. C. B., Kato, S., Minnis, P., Winker, D. M., Liu, G., and Kulesa, C.: Where Is the Best Site on Earth? Domes A, B, C, and F, and Ridges A and B, Publications of the Astronomical Society of the Pacific, 121, 976–992, https://doi.org/10.1086/605780, 2009.

485   Seefeldt, M. W., Cassano, J. J., and Nigro, M. A.: A Weather-Pattern-Based Approach to Evaluate the Antarctic Mesoscale Prediction System (AMPS) Forecasts: Comparison to Automatic Weather Station Observations, Weather and Forecasting, 26, 184–198, https://doi.org/10.1175/2010waf2222444.1, 2011.

Solanki, R., Guo, J., Lv, Y., Zhang, J., Wu, J., Tong, B., and Li, J.: Elucidating the atmospheric boundary layer turbulence by combining UHF radar wind profiler and radiosonde measurements over urban area of Beijing, Urban Climate, 43, 101 151, https://doi.org/10.1016/j.uclim.2022.101151, 2022.

Spinhirne, J. D., Palm, S. P., and Hart, W. D.: Antarctica cloud cover for October 2003 from GLAS satellite lidar profiling, Geophysical Research Letters, 32, https://doi.org/10.1029/2005GL023782, 2005.

Swain, M. and Gallée, H.: Antarctic Boundary Layer Seeing, Publications of the Astronomical Society of the Pacific, 118, 1190–1197, https://doi.org/10.1086/507153, 2006.

Town, M. S. and Walden, V. P.: Surface energy budget over the South Pole and turbulent heat fluxes as a function of an empirical bulk Richardson number, Journal of Geophysical Research, 114, https://doi.org/10.1029/2009jd011888, 2009.

Travouillon, T., Ashley, M. C. B., Burton, M. G., Storey, J. W. V., and Loewenstein, R. F.: Atmospheric turbulence at the South Pole and its implications for astronomy, Astronomy and Astrophysics, 400, 1163–1172, https://doi.org/10.1051/0004-6361:20021814, 2003.

Trinquet, H., Agabi, A., Vernin, J., Azouit, M., Aristidi, E., and Fossat, E.: Nighttime Optical Turbulence Vertical Structure above Dome C in Antarctica, Publications of the Astronomical Society of the Pacific, 120, 203–211, https://doi.org/10.1086/528808, 2008.

Troen, I. B. and Mahrt, L.: A simple model of the atmospheric boundary layer; sensitivity to surface evaporation, Boundary-Layer Meteorology, 37, 129–148, https://doi.org/10.1007/BF00122760, 1986.

Verma, M. K., Kumar, A., and Pandey, A.: Phenomenology of buoyancy-driven turbulence: recent results, New Journal of Physics, 19, 025 012, https://doi.org/10.1088/1367-2630/aa5d63, 2017.

Vernin, J., Chadid, M., Aristidi, E., Agabi, A., Trinquet, H., and Van der Swaelmen, M.: First single star scidar measurements at Dome C, Antarctica, Astronomy and Astrophysics, 500, 1271–1276, https://doi.org/10.1051/0004-6361/200811119, 2009.

Vázquez B, G. E. and Grejner-Brzezinska, D. A.: GPS-PWV estimation and validation with radiosonde data and numerical weather prediction model in Antarctica, GPS Solutions, 17, 29–39, https://doi.org/10.1007/s10291-012-0258-8, 2012.

Wille, J. D., Bromwich, D. H., Nigro, M. A., Cassano, J. J., Mateling, M., Lazzara, M. A., and Wang, S.-H.: Evaluation of the AMPS Boundary Layer Simulations on the Ross Ice Shelf with Tower Observations, Journal of Applied Meteorology and Climatology, 55, 2349–2367, https://doi.org/10.1175/jamc-d-16-0032.1, 2016.

Wille, J. D., Bromwich, D. H., Cassano, J. J., Nigro, M. A., Mateling, M. E., and Lazzara, M. A.: Evaluation of the AMPS Boundary Layer Simulations on the Ross Ice Shelf, Antarctica, with Unmanned Aircraft Observations, Journal of Applied Meteorology and Climatology, 56, 2239–2258, https://doi.org/10.1175/jamc-d-16-0339.1, 2017.

Xie, B., Fung, J. C. H., Chan, A., and Lau, A.: Evaluation of nonlocal and local planetary boundary layer schemes in the WRF model, Journal of Geophysical Research: Atmospheres, 117, n/a–n/a, https://doi.org/10.1029/2011jd017080, 2012.

Xue, H., Giorgetta, M. A., and Guo, J.: The daytime trapped lee wave pattern and evolution induced by two small-scale mountains of different heights, Quarterly Journal of the Royal Meteorological Society, 148, 1300–1318, https://doi.org/10.1002/qj.4262, 2022.

Yagüe, C., Maqueda, G., and Rees, J. M.: Characteristics of turbulence in the lower atmosphere at Halley IV station, Antarctica, Dynamics of Atmospheres and Oceans, 34, 205–223, https://doi.org/10.1016/S0377-0265(01)00068-9, 2001.

Yang, Q., Wu, X., Han, Y., Qing, C., Wu, S., Su, C., Wu, P., Luo, T., and Zhang, S.: Estimating the astronomical seeing above Dome A using Polar WRF based on the Tatarskii equation, Optics Express, 29, 44 000–44 011, https://doi.org/10.1364/oe.439819, 2021.

Yang, Q., Wu, X., Wang, Z., Hu, X., Guo, Y., and Qing, C.: Simulating the night-time astronomical seeing at Dome A using Polar WRF, Monthly Notices of the Royal Astronomical Society, 515, 1788–1794, https://doi.org/10.1093/mnras/stac1930, 2022.

525 Yin, J., Liu, H., Huang, R., Gao, Z., and Wei, Z.: Performance of a PPM hard decision-based ARQ-FSO system in a weak turbulence channel, Chinese Optics Letters, 15, 060 101–60 106, https://doi.org/10.3788/col201715.060101, 2017.

Zhang, J., Guo, J., Xue, H., Zhang, S., Huang, K., Dong, W., Shao, J., Yi, M., and Zhang, Y.: Tropospheric Gravity Waves as Observed by the High-Resolution China Radiosonde Network and Their Potential Sources, Journal of Geophysical Research: Atmospheres, 127, e2022JD037 174, https://doi.org/10.1029/2022JD037174, 2022a.

530 Zhang, J., Guo, J., Zhang, S., and Shao, J.: Inertia-gravity wave energy and instability drive turbulence: evidence from a near-global high-resolution radiosonde dataset, Climate Dynamics, 58, 2927–2939, https://doi.org/10.1007/s00382-021-06075-2, 2022b.

Zuev, V. V. and Savelieva, E.: The cause of the strengthening of the Antarctic polar vortex during October–November periods, Journal of Atmospheric and Solar-Terrestrial Physics, 190, 1–5, https://doi.org/10.1016/j.jastp.2019.04.016, 2019a.

Zuev, V. V. and Savelieva, E.: The cause of the spring strengthening of the Antarctic polar vortex, Dynamics of Atmospheres and Oceans,
535 87, https://doi.org/10.1016/j.dynatmoce.2019.101097, 2019b.